Filling- and interaction-modulated pairing symmetry in twisted bilayer graphene

Jie Cao,[1,*] Fenghua Qi,[2,*] Yuanyuan Xiang [1] and Guojun Jin[3,4,†]

[1]*College of Science, Hohai University, Nanjing 210098, China*

[2]*School of Electronic Engineering, Nanjing Xiaozhuang University, Nanjing 211171, China*

[3]*School of Physics Science and Technology, Kunming University, Kunming 650214, China*

[4]*National Laboratory of Solid State Microstructures, Department of Physics, and Collaborative Innovation Center of Advanced Microstructures, Nanjing University, Nanjing 210093, China*

Superconductivity in twisted bilayer graphene has attracted much attention in recent years. Based on the significant experimental facts, there are many theoretical investigations on its superconducting mechanism and pairing symmetry. In this paper, we study the theory of the electron-phonon coupling in magic-angle twisted bilayer graphene starting from the work of Lian *et al.* [Phys. Rev. Lett. **122**, 257002 (2019)] and thereby develop a uniform framework for the low as well as high electron densities. From this beneficial approach, we obtain the strongest superconductivity near the moiré band filling factor $|\nu| \approx 2$, consistent with the experimental results. By associating it with the Coulomb interaction, we find that the pairing symmetry is strongly dependent on the filling factor, with the p-wave, f-wave, and s-wave pairing states sequentially appearing. It can be confirmed that the superconductivity mostly exists near the half filling of the lowest flat bands with an f-wave pairing symmetry. We discuss the possible origin of these phenomena, the stability of the superconductivity, and also the feasible experimental verification.

I. INTRODUCTION

Twisted bilayer graphene with an accurately controlled twist angle θ has recently emerged as a powerful platform to study the superconductivity and strongly correlated Mott insulating states [1–4]. A twisted graphene bilayer (TGB) is constructed with two rotationally stacked graphene monolayers (GMLs); near the so-called magic angle, two nearly flat bands close to the neutrality point are separated from other higher-energy bands [5–15]. This discovery has revived the hope of unveiling the origin of superconductivity in high-T_c materials, which is one of the long-standing puzzles in strongly correlated electron systems. Traditionally, it has been expected that the strong Coulomb interaction, which is much larger than the kinetic energy of an electron when the carrier density is lower and the Fermi level lies within the flat bands, can drive the system into various phases. The amount of theoretical work has surged on this subject for the purpose of explaining exotic phenomena [16–26].

Although correlated effects have been observed in several moiré systems, robust superconductivity has been reported only in magic-angle twisted graphene bilayer and trilayer systems [27–29]. This fact suggests that the correlated effects and superconductivity come from different origins. Although theoretical consensus is not yet reached regarding the mechanisms underlying the insulating and superconductivity states, more and more experimental evidence indicates that superconductivity may arise through electron-phonon coupling [30–33]. For instance, it is found in experiments that when the Coulomb interaction is weakened by screening, the stability of superconductivity at the optimal doping is enhanced [33]. Several theoretical models have been studied based on the electron-phonon coupling mechanism [34–40], and some experimental facts can be explained. Especially, Ref. [36] points out that a TGB moiré system exhibits an enhanced electron-phonon coupling which makes the conventional superconductivity more favorable at the first magic angle. Even though Ref. [36] provides pronounced results of Bardeen-Cooper-Schrieffer (BCS) superconductivity in a TGB, it is a pity that the electron-phonon coupling Hamiltonian was treated differently for low and high electron densities.

In this paper, we develop the theory of electron-phonon coupling in a TGB in three steps. (1) We derive the analytical electron-phonon coupling term from the deviation of the continuum Hamiltonian without distinction in terms of electron density. The key issue is to transform the Hamiltonian from position space to momentum space. By successfully doing so, we derive the phonon-induced interaction between two electrons and the BCS superconductivity for any electron density. During numerical calculations, it can be shown that the phonon-induced electron-electron coupling is attractive and anisotropic. This coupling alone will introduce an s-wave superconductivity in the TGB. (2) We introduce an isotropic Coulomb interaction into the system due to the small bandwidth of the lowest bands. Combined with the phonon-induced interaction, when the s-wave superconductivity diminishes, an f-wave superconductivity emerges near

*These authors contributed equally to this work.

†Corresponding author: gjin@nju.edu.cn

the filling factor $|\nu| \approx 2$, which is the number of electrons (or holes) filled in a moiré unit cell. It is well known that the f-wave pairing potential is an odd function of momentum similar to a spin-triplet superconductor or superfluid, such as ^{3}He. The appearance of the f-wave superconductivity is due to the repulsive nature of the total coupling, and the gap function must change its sign across the Fermi surface. With an increase in the strength of the Coulomb interaction, the transition temperature for the region $1.5 < \nu < 3$ is stabilized to a certain value, while in other regions the transition temperature quickly drops to zero. This is consistent with the experimental results showing that superconductivity is most likely to appear around the filling factor $\nu \approx 2$. Actually, both the filling factor and the Coulomb interaction can be continuously modulated in experiment by a gate voltage and proximity screening of the substrate [30,31], and the values fall within the parameter space of our calculations. (3) We obtain the solution of pairing symmetries for different filling factors. It is found that the BCS superconductivity can exhibit different symmetry functions when the filling factor varies. Near $|\nu| = 2$, the superconductivity exhibits the f-wave feature, while at low or high filling the pairing symmetry is p wave or s wave. It is important to note that we do not address the Mottness at integer fillings, which is beyond the realm of the BCS theory.

The remainder of this paper is structured as follows. In Sec. II, we briefly review the effective continuum model for a TGB and the lattice-distortion-induced momentum deformation. We obtain the electron-phonon coupling Hamiltonian from the deviation of the full Hamiltonian and derive the equation for the BCS superconducting symmetry function at any filling factor. In Sec. III, we obtain the superconducting gap function near $|\nu| = 2$ and find unusual pairing symmetry. Finally, we give a brief conclusion in Sec. IV.

II. MODEL AND FORMALISM

A. Review of the continuum model

We construct a TGB by rotating layer 1 and layer 2 with angles $-\theta/2$ and $+\theta/2$, respectively, in a totally overlapping graphene bilayer. In the TGB, the lattice constant is $L = a/2\sin(\theta/2)$, where a is the lattice constant of each GML. In momentum space, as shown in Figs. 1(a) and 1(b), the two Dirac points of the rotated graphene layers are separated by $k_\theta = 2K_0 \sin(\theta/2)$, where $K_0 = 4\pi/3a$.

When the twist angle θ is small, the low-energy band structure can be described by the Dirac model around the Dirac points of a monolayer, where the intervalley mixing can be safely neglected. For a single valley, taking $\xi = +$ as an example, we can write the Hamiltonian with the interlayer coupling by the moiré potential $T(\mathbf{r})$ [5,9], that is,

$$H_e^+ = \begin{pmatrix} -i\hbar v_F \boldsymbol{\sigma}_{\theta/2} \cdot \nabla & T(\mathbf{r}) \\ T^\dagger(\mathbf{r}) & -i\hbar v_F \boldsymbol{\sigma}_{-\theta/2} \cdot \nabla \end{pmatrix}, \quad (1)$$

where $\boldsymbol{\sigma}_{\theta/2} = e^{-(i\theta/4)\sigma_z}(\sigma_x, \sigma_y)e^{(i\theta/4)\sigma_z}$, $\nabla = (\partial_x, \partial_y)$, and $T(\mathbf{r}) = \sum_{j=1}^{3} T_j e^{-i\mathbf{q}_j \cdot \mathbf{r}}$. The three-momentum transfers $\mathbf{q}_j$ are $\mathbf{q}_1 = k_\theta(0, -1)$, $\mathbf{q}_2 = k_\theta(\sqrt{3}/2, 1/2)$, and $\mathbf{q}_3 = k_\theta(-\sqrt{3}/2, 1/2)$, as shown in Fig. 1(c).
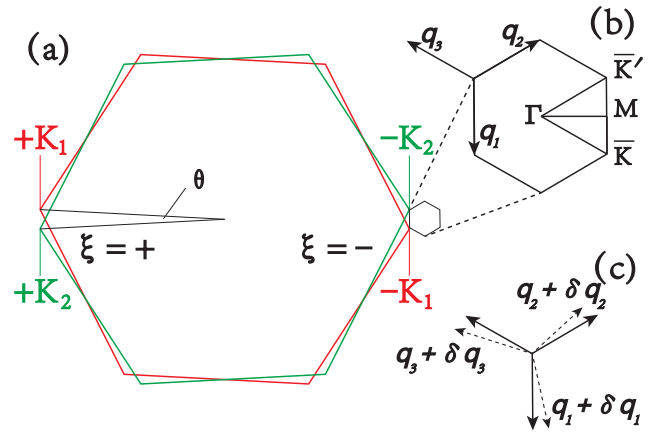

FIG. 1. (a) Brillouin zone folding in the TGB with a small twist angle θ. The two large hexagons represent the first Brillouin zones (BZs) of the two GMLs distinguished by red (layer 1) and green (layer 2), with $\pm K_{1,2}$ as the valleys in the BZs. (b) The small hexagon is the moiré Brillouin zone (MBZ) of the TGB, with $\overline{K}$ and $\overline{K}'$ as the valleys in the MBZ. The three $\mathbf{q}_j$ are the momentum transfers that correspond to the three interlayer hopping processes. (c) Under lattice deformations, $\mathbf{q}_j$ are distorted in the momentum space.

The symmetry of the TGB requires the interlayer coupling to have the form

$$T_j = w_{AA}\sigma_0 + w_{AB}[\sigma_x \cos(j-1)\phi + \sigma_y \sin(j-1)\phi], \quad (2)$$

where $\phi = 2\pi/3$ and w_{AA} and w_{AB} are the interlayer hopping parameters in the AA and AB stacking regions. Throughout this paper we take $\hbar v_F = \sqrt{3}at/2$, where $t = 2.6$ eV is the hopping energy between the nearest-neighbor atoms on a graphene layer, and we fix $\omega_{AA} = 0.08$ eV and $\omega_{AB} = 0.1$ eV [41].

The Hamiltonian for the other valley, $\xi = -$, can be easily obtained by applying a time-reversal transformation to H_e^+. Since our model preserves the particle-hole-like symmetry which transforms H_e^+ into $-H_e^-$, we focus on the particle side where the filling factor $\nu > 0$.

B. Momentum deformation caused by lattice distortion

When small distortions are applied on the TGB lattice, the change in the related momenta is schematically shown in Fig. 1(c). Denoting the in-plane atom displacement field of layer l ($l = 1, 2$) at $\mathbf{r}$ as $\mathbf{u}^{(l)}(\mathbf{r}) = (u_x^{(l)}(\mathbf{r}), u_y^{(l)}(\mathbf{r}))$, the variation of the momentum transfer $\mathbf{q}_j$ [36] is given as

$$\delta\mathbf{q}_j = k_\theta \gamma \nabla F_j(\mathbf{r}) + k_\theta \nabla G_j(\mathbf{r}),$$
$$F_j(\mathbf{r}) = u_x \cos(j-1)\phi + u_y \sin(j-1)\phi,$$
$$G_j(\mathbf{r}) = -u_x^c \sin(j-1)\phi + u_y^c \cos(j-1)\phi, \quad (3)$$

where we define $\gamma = [2\tan(\theta/2)]^{-1}$, the relative displacement field $\mathbf{u} = \mathbf{u}^{(1)} - \mathbf{u}^{(2)}$, and the center-of-mass displacement field $\mathbf{u}^c = (\mathbf{u}^{(1)} + \mathbf{u}^{(2)})/2$. For small angle θ, $\delta\mathbf{q}_j$ is dominated by the relative displacement phonon field $\mathbf{u}$ since $\gamma \gg 1$. This can be understood from the fact that a uniform relative displacement $\mathbf{u}$ yields a significant displacement of the AA stacking positions by $\gamma|\mathbf{u}|$ perpendicular to $\mathbf{u}$ [42–44].

If the relative displacement $\boldsymbol{u}$ is nonuniform, it will induce a large superlattice deformation due to the amplification factor γ. Accordingly, the low-energy electrons will experience a strong coupling with the in-plane relative displacement phonon field $\boldsymbol{u}$.

While the momentum vectors $\boldsymbol{q}_j$ are distorted by the phonon field, the interlayer coupling matrices T_j remain unaffected. This can be understood as follows: The continuum model captures the most essential properties in the moiré potential, i.e., the interlayer coupling forms in the AA, AB, and BA regions are exact. Even though the moiré pattern is significantly changed by the phonon field, the exact interlayer coupling forms in the new AA, AB, and BA regions require the interlayer coupling matrices T_j to be unchanged. Therefore, in the continuum model Hamiltonian, only $\boldsymbol{q}_j$ is changed under the deformation. We ignore the second term in $\delta\boldsymbol{q}_j$ hereinafter

and focus on the coupling between the low-energy electrons and the in-plane relative displacement phonon field $\boldsymbol{u}$.

C. Electron-phonon coupling Hamiltonian

Since the momentum deformations can be expressed using the phonon fields, the change in the continuum model Hamiltonian H_e^+ gives the low-energy electron-phonon coupling term, namely,

$$H_{ep}^+ = H_e^+(\boldsymbol{q}_j + \delta\boldsymbol{q}_j) - H_e^+(\boldsymbol{q}_j). \tag{4}$$

However, we can see that the change in the moiré potential cannot be transformed to the momentum space by expanding $\delta T(\boldsymbol{r}) \approx -i \sum_{j=1}^{3} T_j e^{-i\boldsymbol{q}_j \cdot \boldsymbol{r}} \delta\boldsymbol{q}_j \cdot \boldsymbol{r}$ to the linear order of $\delta\boldsymbol{q}_j \cdot \boldsymbol{r}$. Hence we solve this problem in the momentum space.

In the momentum space, the electron Hamiltonian has infinite dimensions:

$$H_e^+(\boldsymbol{k}) = \begin{pmatrix} h(\boldsymbol{k}) & U_1 & U_2 & & & \\ U_1^\dagger & h(\boldsymbol{k} - \boldsymbol{q}_1) & 0 & & & \\ U_2^\dagger & 0 & h(\boldsymbol{k} - \boldsymbol{q}_2) & 0 & & \cdots \\ & & 0 & \ddots & & \\ & & \vdots & & h(\boldsymbol{k} - \boldsymbol{q}_n) & \\ & & & & & \ddots \end{pmatrix}, \tag{5}$$

where $h(\boldsymbol{k}) = \hbar v_F \boldsymbol{\sigma} \cdot \boldsymbol{k}$ is the Dirac Hamiltonian of the GML. The dependence of $h(\boldsymbol{k})$ on angle is parametrically small and can be neglected for the first magic angle. $\boldsymbol{q}_n = \sum_j m_j^n \boldsymbol{q}_j$ is the possible combinations of $\boldsymbol{q}_j$, where m_j^n are integer numbers. When the phonon fields are considered, the variation of the Hamiltonian $H_e^+(\boldsymbol{k})$, i.e., the electron-phonon coupling term, is simply given as $H_{ep}^+ = -\text{diag}[0, h(\delta\boldsymbol{q}_1), h(\delta\boldsymbol{q}_2), \ldots, h(\delta\boldsymbol{q}_n), \ldots]$. For low electron density, this Hamiltonian can be truncated to a 4×4 block matrix which can be treated analytically. For high electron density, however, the pattern of $\delta\boldsymbol{q}_n$ is unclear. One of our main contributions in this paper is to find a way to relate $\delta\boldsymbol{q}_n$ to the known pattern of $\boldsymbol{q}_n$.

By rotating $\boldsymbol{q}_j$ by $90°$, i.e., $\hat{z} \times \boldsymbol{q}_j = k_\theta(\cos(j-1)\phi, \sin(j-1)\phi)$, we have $(\hat{z} \times \boldsymbol{q}_j/k_\theta) \cdot \boldsymbol{u} = F_j(\boldsymbol{r})$. Hence the variation of the momentum transfer $\boldsymbol{q}_j$ is expressed as

$$\delta\boldsymbol{q}_j = \gamma \nabla(\boldsymbol{u} \cdot (\hat{z} \times \boldsymbol{q}_j)). \tag{6}$$

Furthermore, since $\boldsymbol{q}_n$ is the linear combinations of $\boldsymbol{q}_j$, the variation of $\boldsymbol{q}_n$ is finally given as

$$\delta\boldsymbol{q}_n = \gamma \nabla(\boldsymbol{u} \cdot (\hat{z} \times \boldsymbol{q}_n)). \tag{7}$$

D. The BCS electron-electron interaction

In the TGB system the interlayer van der Waals interaction between two GMLs is much weaker than the intralayer atomic interaction, and the in-plane polarized phonons of the two GMLs are nearly decoupled [45,46]. The phonon bands in the MBZ are simply obtained by folding the phonon bands of the GMLs into the superlattice MBZ, and the long-wavelength

relative displacement phonon field is combined from the GML phonon field given by

$$\boldsymbol{u}(\boldsymbol{r}) = \sum_{\boldsymbol{p}} \frac{e^{i\boldsymbol{p}\cdot\boldsymbol{r}}}{\sqrt{N_s \Omega_s}} (i\hat{\boldsymbol{p}} u_{\boldsymbol{p},L} + i\hat{z} \times \hat{\boldsymbol{p}} u_{\boldsymbol{p},T}),$$

$$u_{\boldsymbol{p},L/T} = \sqrt{\frac{\hbar\Omega}{2M\omega_{\boldsymbol{p},L/T}}}(a_{\boldsymbol{p},L/T} + a_{-\boldsymbol{p},L/T}^\dagger), \tag{8}$$

where $N_s \Omega_s$ is the area of the sample, $\hat{\boldsymbol{p}} = \boldsymbol{p}/p$ is the unit vector along momentum $\boldsymbol{p}$, $\hat{z}$ is the unit vector along the out-of-plane direction, and Ω is the area of the unit cell of the GML. There are two in-plane acoustic phonon eigenmodes, namely, the longitudinal ($u_{\boldsymbol{p},L}$) and transverse ($u_{\boldsymbol{p},T}$) modes; M and $\omega_{\boldsymbol{p},L/T}$ are the atom mass and the eigenmode frequency; and $a_{\boldsymbol{p},L/T}$ and $a_{\boldsymbol{p},L/T}^\dagger$ are the phonon annihilation and creation operators.

Finally, the matrix element of the electron-phonon coupling Hamiltonian can be written as

$$\langle\boldsymbol{k}|H_{ep}^+|\boldsymbol{k}'\rangle = -\frac{\hbar v_F \gamma p \sqrt{\hbar\Omega}}{\sqrt{2M\omega_p N_s \Omega_s}} \langle\boldsymbol{k}|A^+(\boldsymbol{p})|\boldsymbol{k}'\rangle, \tag{9}$$

where $A^+(\boldsymbol{p}) = \text{diag}(0, \ldots, A_n^+(\boldsymbol{p}), \ldots)$ and

$$A_n^+(\boldsymbol{p}) = e^{i\boldsymbol{p}\cdot\boldsymbol{r}}\boldsymbol{\sigma} \cdot \hat{\boldsymbol{p}}[\hat{\boldsymbol{p}} \cdot (\hat{z} \times \boldsymbol{q}_n)(a_{\boldsymbol{p},L} + a_{-\boldsymbol{p},L}^\dagger)$$

$$+ \hat{\boldsymbol{p}} \cdot \boldsymbol{q}_n(a_{\boldsymbol{p},T} + a_{-\boldsymbol{p},T}^\dagger)], \tag{10}$$

where $|\boldsymbol{k}\rangle$ and $|\boldsymbol{k}'\rangle$ are the eigenstates of H_e^+, $\boldsymbol{p} = \boldsymbol{k} - \boldsymbol{k}'$, and we assume $\omega_{\boldsymbol{p},L} \approx \omega_{\boldsymbol{p},T} = \omega_p$. It is worth noticing that Eq. (10) describes the electron-phonon coupling in the

$\xi = +$ valley, while in the $\xi = -$ valley the electron-phonon coupling Hamiltonian can be obtained using the time-reversal transformation.

We now calculate the phonon-mediated electron-electron interaction near the Fermi surface. We do not necessarily

$$\frac{V_{k,k'}}{\Omega_s} = \frac{\hbar^2 \gamma^2 v_F^2 \Omega}{2MC^2 \Omega_s} \frac{\hbar^2 \omega_p^2}{\hbar^2 \omega^2 - \hbar^2 \omega_p^2} \sum_{\chi = L,T} \langle k'^\xi, -k'^{\bar{\xi}} | A^{\bar{\xi}}(p) | k'^\xi, -k^{\bar{\xi}}, p_\chi \rangle \langle k'^\xi, -k^{\bar{\xi}}, p_\chi | A^\xi(p) | k^\xi, -k^{\bar{\xi}} \rangle. \tag{11}$$

Together with Eq. (10), we can obtain the expression for the electron-electron interaction. Accordingly, in the second quantization language, the phonon-mediated electron-electron interaction in the Cooper channel is

$$H_{\text{int}} = \frac{1}{N_s \Omega_s} \sum_{k,k'} V_{k,k'} c_{k'}^{\dagger \xi} c_{-k'}^{\dagger \bar{\xi}} c_{-k}^{\bar{\xi}} c_k^\xi. \tag{12}$$

The detailed derivation can be found in the Appendix.

E. Competition between the phonon-induced attraction and the Coulomb repulsion

If we confine our considerations to the vicinity of the Fermi surface, the effective electron-electron interaction is most likely to be attractive when $\omega \ll \omega_p$ and BCS superconductivity will occur. From a rough estimation using the realistic system parameters $t = 2.6$ eV, $C \approx 10^4$ m/s, $\theta = 1.05°$, we obtain the interaction strength $V/\Omega_s \approx -1$ meV, which is comparable to the superconductivity transition temperature in experiments. The results of the numerical calculations show that the average value of $V_{kk'}$ across the BZ is about 1.08 meV; however, the variation of $V_{kk'}$ is relatively large. The maximum of $V_{kk'}$ can reach 3 meV, while the minimum of $V_{kk'}$ approaches zero. On the other hand, due to the flatness of the lowest conduction or highest valence band, the Coulomb repulsion is non-negligible. It is reasonable to consider that the screened Coulomb interaction strength is of the order of 10 meV. Afterwards, we will consider a uniform effective Coulomb repulsion as well as the phonon-mediated attraction. Even though the Coulomb interaction is much stronger than the phonon-induced electron-electron coupling, the superconductivity is not utterly suppressed in this system. If the attraction is also uniform, i.e., introduces an isotropic s-wave superconductivity, the Coulomb interaction will decrease the critical temperature and even destroy the superconductivity. However, if the attraction is anisotropy along the Fermi surface, the Coulomb interaction can reverse the sign of the interaction on parts of the Fermi surface. In this case, the leading symmetry of the superconductivity will change.

Normally, a uniform Coulomb interaction term can be written as

$$H_c = \frac{U}{N_s \Omega_s} \sum_{k,k'} c_{k'}^{\dagger \xi} c_{-k'}^{\dagger \bar{\xi}} c_{-k}^{\bar{\xi}} c_k^\xi, \tag{13}$$

assume that the Fermi surface is near the Dirac points, and the following procedure can be performed at any electron filling. Using the standard second-order perturbation theory, we obtain the BCS electron-electron interaction as

and the total interaction Hamiltonian in the Cooper channel can become

$$H_{\text{total}} = \frac{1}{N_s \Omega_s} \sum_{k,k'} (U + V_{k,k'}) c_{k'}^{\dagger \xi} c_{-k'}^{\dagger \bar{\xi}} c_{-k}^{\bar{\xi}} c_k^\xi. \tag{14}$$

The superconductivity could be contributed by the lowest four separated moiré bands (two per valley). Therefore, in principle, we should consider all of them and calculate both the intra- and interband pairing. However, the zero-frequency pairing susceptibility is proportional to $(\varepsilon_{k_1} + \varepsilon_{k_2} - 2E_f)^{-1}$, where ε_k is the energy dispersion of the lowest bands. Without considering the modulation of the bands by interaction, the conduction band and the valence band are energetically separated from each other. Therefore the energy difference of the two electrons from different bands is relatively big, so that the contribution from interband pairing can be safely ignored. Here, we only retain the first conduction band for simplicity. With the mean-field approximation, the self-consistency gap equation [47] is given as

$$\Delta(k) = \sum_{k'} \chi_{k,k'} \Delta(k'),$$

$$\chi_{k,k'} = \frac{U + V_{k,k'}}{2N_s \Omega_s} \frac{\tanh \frac{\varepsilon(k') - E_F}{2k_B T}}{\varepsilon(k') - E_F}. \tag{15}$$

The transition temperature T_c is determined by the highest T such that χ yields an eigenvalue of 1.

To be more concrete, we only treat Eq. (15) along the Fermi surface, i.e., $\varepsilon(k') \approx E_F$. We decompose the superconducting gap into an amplitude Δ and a normalized symmetry function $g(k)$ and define a dimensionless pairing strength function as

$$\lambda[g(k)] = -\frac{\oint_C \frac{dk}{v(k)} \oint_{C'} \frac{dk'}{v(k')} g(k)(U + V_{k,k'}) g(k')}{(2\pi)^2 \oint_C \frac{dk}{v(k)} [g(k)]^2}, \tag{16}$$

where the integral $\oint_{C(C')}$ is along the momentum path defined on the Fermi surface in the ξ valley and $v(k) = \frac{1}{\hbar} |\nabla_k \varepsilon_k|$ is the corresponding Fermi velocity. From the stationary condition, we derive the following generalized eigenequation:

$$-\oint_{C'} \frac{dk'}{(2\pi)^2 v(k')} (U + V_{k,k'}) g_\alpha(k') = \lambda_\alpha g_\alpha(k). \tag{17}$$

This is our fundamental theoretical formula, from which we can get the leading pairing function. There are two common methods to solve Eq. (17). One is to decompose the pairing interaction vertex $\Gamma_{k,k'} = U + V_{k,k'}$ in momentum space to selected pairing channels with different pairing symmetries

allowed by group symmetry. In this way, the pairing channels are always restricted to the leading angular harmonics for simplification. The gap function can be recovered by the eigenvector corresponding to the most positive eigenvalue.

The other method (which we adopted in this paper) is to project the pairing interaction to the Fermi surface and solve the reduced eigenproblem. In this procedure, no pairing symmetries are excluded beforehand. The gap function with the most positive eigenvalue corresponds to the highest possible pairing symmetry. The eigenvalue λ is to be related to the transition temperature as $T_c \approx \Lambda_0 e^{-1/\lambda}$, where Λ_0 is an energy scale. Hence the largest eigenvalue will lead to the highest superconducting transition temperature, and its eigenfunction determines the symmetry of the gap. In the BCS framework, the advantage of this method is that it considers only the states near the Fermi surface and greatly simplifies the calculations.

III. RESULTS AND DISCUSSION

A. The f-wave superconductivity near $\nu = 2$

One of the main results we obtain here is that the superconducting gap near the filling $\nu = 2$ has an f-wave symmetry during the normal-metal–superconductor phase transition with the presence of both the phonon-induced electron-electron attraction and the Coulomb repulsion. In Figs. 2(a) and 2(b), we calculate and plot the BCS superconducting gap function $g(\boldsymbol{k})$ on the Fermi surface at $\nu = 2.1$ for $U = 0$ and $U = 2$ meV; the color from red to blue denotes the positive to negative sign of the gap function. In the $U = 0$ case, the phonon-induced electron-electron coupling is purely attractive, and the BCS superconducting gap has a normal s-wave symmetry. However, in the $U = 2$ meV case, our results show that the BCS superconducting gap for the first-magic-angle TGB exhibits the unique symmetry that the gap function changes sign six times, with six 0 nodes, along the Fermi surface; this is the f-wave symmetry. Previous research [38,40] has argued for the presence of f-wave pairing in the trilayer system based on the sublattice space classification of the pairings. In that research, the intrasublattice (s- or f-wave) pairing and the intersublattice (p- or d-wave) pairing were assigned in advance.

It should be pointed out that the pairing potential in the position space does not have explicit dependence on momentum. This is unusual since the spin-triplet pairing potential should be an odd function of momentum. In our research, we do not preassume any preferred symmetry, and the momentum-dependent f-wave pairing gap naturally emerges along with the disappearance of the s-wave symmetry. In the C_{3v} point group, the s-wave and f-wave symmetries belong to the same irreducible representation A_1; hence the f-wave symmetry is favorable when the repulsion U destroys the s-wave symmetry.

In order to give a better description, we restrict ourselves to finding the smallest number of harmonics necessary for a reasonable fit of the pairing symmetry solution which has the $\boldsymbol{k}$ dependence. It is in the form

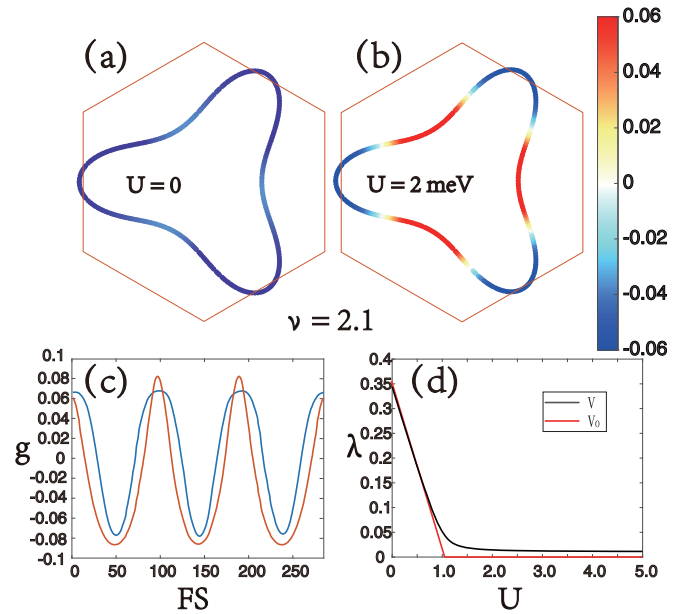$$g^f(\boldsymbol{k}) = g_0^f \sin k_x \big(\sin k_x^2 - 3 \sin k_y^2 \big), \qquad (18)$$

FIG. 2. (a) and (b) The numerical results of the phonon-induced BCS superconducting gap function at $\nu = 2.1$. Six gap nodes are found along the highly symmetric curve for $U = 2$ meV. (c) The f-wave symmetry gap function $g(\boldsymbol{k})$ along the Fermi surface (FS); the x axis is the number of the points along the FS. We compare a fit of $g(\boldsymbol{k})$ (blue curve) with the numerical values of $g(\boldsymbol{k})$ (red curve). It is clear that the fit function captures the essential feature of $g(\boldsymbol{k})$. (d) The transition temperature, i.e., λ, changes with the increase in the Coulomb interaction strength U. For the anisotropic case (black curve), λ drops quickly when U exists initially. However, λ is stabilized at 0.03 when U exceeds 2 meV. On the other hand, if we choose $V_{\boldsymbol{k},\boldsymbol{k}'} = V_0 = 1.08$ meV for the isotropic case (the red curve), λ drops to zero rapidly, which means that the Coulomb interaction destroys the s-wave superconductivity completely.

where g_0^f is the normalization constant. In Fig. 2(c) we show the f-wave symmetry function $g(\boldsymbol{k})$ along the Fermi surface at $\nu = 2.1$. We compare the fit (blue curve) with the numerically calculated values of $g(\boldsymbol{k})$ (red curve). It can be seen that the fit captures the main feature of $g(\boldsymbol{k})$. The pairing symmetry solution for the s-wave pairing has an anisotropic feature that is similar to that of the f-wave $g(\boldsymbol{k})$ pairing. This may stem from their common irreducible representation A_1. Using the analytical expression of $g(\boldsymbol{k})$, the f-wave pairing symmetry can be experimentally detected by the field-angle dependence of the transport and thermodynamical quantities.

In addition, one can find the solutions of the largest pairing eigenvalues and pairing eigenfunctions for different Coulomb interaction strengths. In Fig. 2(d) we plot the variation of λ with the increase in the Coulomb interaction from $U = 0$ to $U = 5$ meV. We find that in the region $0 < U < 1$ meV, there is an s-wave pairing solution and that otherwise the pairing symmetry is of f-wave type. We notice that the Coulomb repulsion does not destroy the superconductivity. Instead, as U increases, both $g(\boldsymbol{k})$ and λ are stabilized at certain values. In Fig. 2(d), we can see that when $U > 2$ meV, λ becomes almost invariant. As a comparison, in the isotropic case, i.e., $V_{\boldsymbol{k},\boldsymbol{k}'} = -V_0$, where V_0 is the average attraction strength, λ rapidly drops to zero when $U > V_0$.
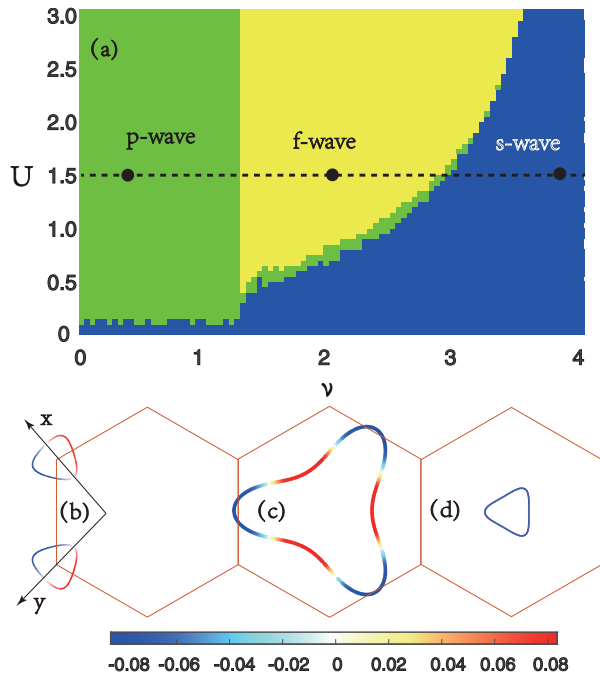
FIG. 3. Pairing symmetry changes with the filling factor. (a) Phase diagram of interaction and filling, in which there are three regions corresponding to p-, f-, and s-wave pairing symmetries. (b) A p-wave pairing at low filling with $U = 1.5$ meV. The Fermi surface splits into two closed parts around the MBZ corners. The two axes are perpendicular to each other. (c) and (d) An f- and an s-wave pairing at moderate and high filling, respectively, with $U = 1.5$ meV. Their Fermi surfaces are singly closed. The three pairing symmetries correspond to the three dots in the phase diagram.

The above phenomena can be understood by a three-patch toy model [22] in which we construct the order parameters $\Delta(\boldsymbol{k}) = \Delta[g(\boldsymbol{Q}_1), g(\boldsymbol{Q}_2), g(\boldsymbol{Q}_3)]^{\mathrm{T}}$. $\boldsymbol{Q}_{j=1,2,3}$ are the main segments on the Fermi surface where $\boldsymbol{Q}_j = C_3^{j-j'}\boldsymbol{Q}_{j'}$ and $g(\boldsymbol{Q}_j)$ reach the maximum (or minimum). Thus $V_{\boldsymbol{k},\boldsymbol{k}'}$ is truncated to a 3×3 matrix, and Eq. (17) is written as

$$\begin{pmatrix} -U + V_0 & -U + V_0 - \delta & -U + V_0 - \delta \\ -U + V_0 - \delta & -U + V_0 & -U + V_0 - \delta \\ -U + V_0 - \delta & -U + V_0 - \delta & -U + V_0 \end{pmatrix} g$$

$$= v(\boldsymbol{Q})\lambda g, \tag{19}$$

where δ represents the anisotropy. Clearly, in this toy model, the maximum value of $\lambda = \delta/v$ keeps unchanged as long as $U \geqslant V_0 - \delta$. Therefore the Coulomb repulsion, no matter how large it is, does not destroy the superconductivity if the anisotropic interaction term $\delta > 0$.

B. Pairing symmetry changes with filling factor

In Fig. 3(a), we plot the U-v phase diagram and distinguish the phase regions by the number of nodes on the Fermi surface. The phase diagram is divided into three regions, where each region represents a uniform superconducting symmetry. In the low-filling region, a small but finite U can lead the system into a p-wave symmetry. By traversing a phase boundary which is a straight line parallel to the U axis, the system enters

into the f-wave symmetry. By checking the Fermi surface we find that this phase boundary corresponds to the transition of the Fermi surface from two separated circles to one united circle around $v \approx 1.3$. Due to the fact that we consider the single-electron band structure in the calculations, U does not change the shape of the Fermi surface. At $v \approx 1.3$ the Fermi surface fuses from two separate ones into a large complete Fermi surface. After this transition, the corresponding quantities such as λ and pairing symmetry experience a sudden change. The other phase boundary of this middle region is determined by the critical value of U at the transition point increasing parabolically with the increase in the filling factor v. After this phase boundary, the system becomes s-wave symmetric. We conclude that the superconductivity symmetry is variable with both the number taken by the filling factor and the strength of the Coulomb interaction.

In the low-filling case, the Coulomb interaction drives the system into a stable p-wave superconducting state. In Fig. 3(b) we calculate the BCS superconducting gap for $v = 0.4$ and $U = 1.5$ meV. The Fermi surface is divided into two parts enclosing the two inequivalent MBZ corners. As illustrated in Fig. 3(b), each Fermi surface exhibits a p-wave symmetry, and the pairing function is antisymmetric about the tilted x and y axes. By projecting onto the new coordinate system, one can fit the p-wave pairing symmetry using the usual p-wave form factor, i.e., $\sin(kx)$ and $\sin(ky)$.

In the moderate-filling case, the Coulomb interaction drives the system into a stable f-wave superconducting state. In Fig. 3(c) we calculate the BCS superconducting gap for $v = 2.1$ and $U = 1.5$ meV. The pairing symmetry is the same as in the previous section.

In the high-filling case, however, the Coulomb interaction does not change the symmetry of the superconductivity. As shown in Fig. 3(d), the symmetry is unchanged for $v = 3.8$ and $U = 1.5$ meV. This is due to the fact that the Fermi surface is concentrated near the Γ point resulting in relatively close wave functions and weak anisotropy of the interactions. When the strength of a uniform Coulomb interaction exceeds that of the average attraction, λ rapidly drops to zero, representing that the Coulomb interaction quenches the superconductivity instead of stabilizing it as in the half-filling case.

C. The most probable region for superconductivity

In Fig. 3, we take the largest eigenvalue for a certain combination of (U, v) and mark the corresponding symmetry in the phase diagram. For clarity, we have shown the variation of λ with v in Fig. 4 for several U using the same criterion as in Fig. 3(a). The higher values of λ give the more probable regions for superconductivity.

We investigate the evolution of the leading eigenvalue λ as a function of the filling factor v and show the numerical results in Fig. 4. The meaningful range of values for v is between 0 and 4. In the case of no Coulomb interaction, we find that the phonon-induced electron-electron coupling is strongest in the region $1.8 < v < 2.8$, which is caused by the largest density of states (DOS) being in this region. In the region $v < 1.8$ and $v > 2.8$, λ drops rapidly due to the reduced DOS. When the Coulomb interaction is present, it can be seen that λ drops very quickly with the increase in U in the region $3.5 < v < 4$,
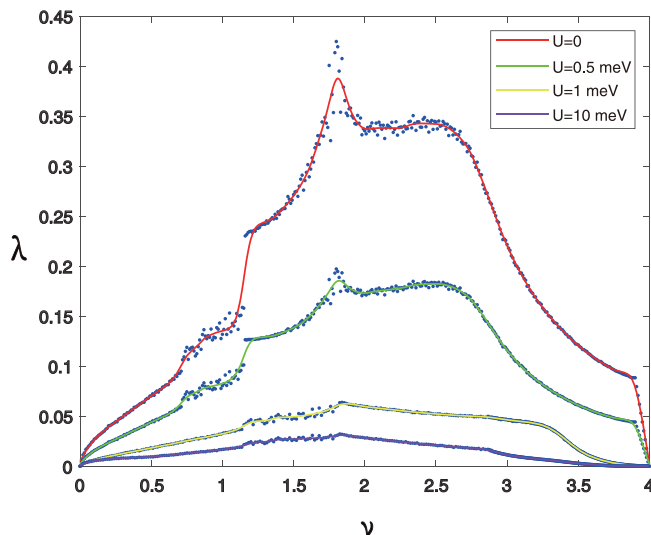
FIG. 4. The leading eigenvalue λ vs filling factor ν for different Coulomb interactions U. Near $\nu = 2$ the eigenvalue reaches its maximum, which means that the superconducting transition temperature reaches its maximum. The disconnected computational results are fitted by solid curves through the numerical fitting approach. The influence of noise on the results can be corrected, and we can still see a peak of λ near $\nu = 2$, which is consistent with experimental measurement.

while in the region $1.5 < \nu < 3$, λ greatly decreases initially when U is added but barely changes when $U > 5$ meV.

This phenomenon can be explained by the result of the previous section. In the region $3.5 < \nu < 4$, the wave functions along the Fermi surface are very similar to each other, and the anisotropy of $V_{k,k'}$ is small. Hence the isotropic Coulomb repulsion U destroys the superconductivity rapidly. However, in the region $1.5 < \nu < 3$, the anisotropy of $V_{k,k'}$ is relatively large, and the superconductivity transition temperature is stabilized when U exceeds a certain value. In the low-filling region $\nu < 1.3$, the superconductivity is stabilized to a p-wave state as λ is relatively small. These results indicate that the superconductivity is most likely to appear around the filling factor $\nu \approx 2$ and the corresponding symmetry is a f-wave pairing symmetry. Away from this region, the transition temperature is seriously dropped as the eigenvalue λ is decreased. This is consistent with the experimental results.

It is a little surprising to find that the values in Fig. 4 are so noisy, and one may ask, What is the main source of uncertainty? On the other hand, the fluctuation of the data points seems to be very correlated across different values of U. In particular, this seems most evident by comparing the data sets $U = \{0, 0.5\}$ meV and $U = \{1, 10\}$ meV. Actually, in the numerical calculations of pairing symmetry, we can only take a finite number of points on the Fermi surface, say, 400, and build a matrix of finite dimension for the numerical solutions. When the filling level changes, we retake other points for calculations. In this process, the discrete points on the Fermi surface obtained from adjacent filling levels are difficult to change continuously, so the numerical results will be slightly noisy. As for the correlation of the data for different U, we can understand it qualitatively. First of all, the overall

superconducting transition temperature is decreasing as U becomes larger. Secondly, at smaller U, a higher peak appears near the half filling, coinciding with the peak of the DOS. In contrast, at larger U, this peak is not obvious, indicating that the superconducting state is highly modulated by Coulomb interaction. The boundary between these two types of data is around $U \sim 0.8$ meV, a value that is also approximately the average strength of electron-phonon interactions. Below this value, the dominant electron-phonon interactions lead to s-wave pairing; above this value, Coulomb interactions begin to dominate and eventually lead to the appearance of the f-wave pairing.

The odd-parity pairing symmetry holds a special interest in the community in pursuit of governing triplet pairing, chiral pairing, topological superconductivity, and Majorana edge modes. It naturally arises in the spin-triplet channel of strongly correlated systems. The f-wave pairing has been suggested in heavy-fermion UPt$_3$ [48,49], monolayer MoS$_2$ [50], the cold-atom optical lattice [51], and other honeycomb lattices [52]. However, it is beneficial that the f-wave pairing in the TGB system requires neither strong correlation nor nesting-induced instability.

IV. CONCLUSIONS

We have developed a superconductivity theory in a twisted graphene bilayer in a uniform framework taking into account the low and high electron densities simultaneously. We have derived an efficient generalized eigenequation and solved it with the phonon-induced effective electron-electron interactions. Combining the filling factor ν among [0,4] with the Coulomb repulsion U, a U-ν phase diagram has been plotted for the superconducting pairing symmetry, where the p-wave, f-wave, and s-wave pairing symmetries are distinguished by different U and ν. We have obtained an unusual f-wave pairing symmetry in the BCS channel and found that the f-wave superconducting gap only appears near $|\nu| \approx 2$, where the superconductivity is confirmed experimentally. We have verified that in the case of no Coulomb interaction, the superconductivity is most favorable in the region $1.8 < |\nu| < 2.8$ with s-wave symmetry. When the Coulomb interaction is turned on, the superconductivity is severely depressed and is stabilized in the region $1.5 < \nu < 3$ as observed in experiments. Furthermore, the superconductivity transition temperature is slightly enhanced when the Coulomb interaction is decreased, which is also consistent with experimental results. We only consider the noninteraction band structure in the calculations; correlation effects such as Hartree deformation of the bands could bring some changes to our results. The Hartree potential contributes to the Hamiltonian of the TGB as a diagonal term in the sublattice or layer subspace; hence the band structure, as well as the DOS, is possibly altered. Previous research shows that the Van Hove singularity is pinned at the Fermi level for a large range of dopings [53]. Since the DOS plays a major role in the electron-phonon interactions, the Hartree potential might increase the value of λ in a large range of filling for small U, with the dominant electron-phonon interactions leading to s-wave pairing. On the other hand, for large U, i.e., away from the s-wave region, Coulomb interactions begin to dominate, and the effect of the DOS change might be less

obvious. The f-pairing gap in our model is an odd function of momentum, and it can be tested by the field-angle signal of the transport experiments or angle-resolved photoemission spectroscopy (ARPES) experiments.

APPENDIX: ELECTRON-ELECTRON INTERACTION MEDIATED BY PHONONS

It is known that the in-plane phonons of the two layers of a TGB are nearly decoupled [45]. Therefore the TGB in-plane phonon spectrum is approximately that of two isolated GMLs folded in the MBZ, and the low-energy acoustic phonon Hamiltonian is

$$H_{ph} = \sum_{\boldsymbol{p}, \chi = L, T} \hbar \omega_{\boldsymbol{p}, \chi} a_{\boldsymbol{p}, \chi}^{\dagger} a_{\boldsymbol{p}, \chi}, \tag{A1}$$

where the frequency $\omega_{\boldsymbol{p}, \chi}$ of the low-energy phonons is linearly proportional to p, i.e., $\omega_{\boldsymbol{p}, L} \approx \omega_{\boldsymbol{p}, T} \approx Cp$. One can follow the standard second-order perturbation theory to calculate the phonon-mediated electron-electron interaction where the electron Hamiltonian H_e^{ξ} and the phonon Hamiltonian H_{ph} are treated as the unperturbed Hamiltonian and H_{ep}^{ξ} is the perturbation term. Consider the initial state $|\Psi_i\rangle = |\boldsymbol{k}_1^{\xi}, \boldsymbol{k}_2^{\xi'}\rangle$ of two electrons which have momenta $\boldsymbol{k}_1$ and $\boldsymbol{k}_2$, respectively, where the spin index is omitted since the electron-phonon coupling term H_{ep}^{ξ} is spin independent. Mediated by the phonon emission and absorption, the initial state is scattered to the final state $|\Psi_f\rangle = |\boldsymbol{k}_3^{\xi}, \boldsymbol{k}_4^{\xi'}\rangle$ through two intermediate states by emitting a phonon with polarization χ: One state is $|\Psi_{1,\chi}\rangle = |\boldsymbol{k}_3^{\xi}, \boldsymbol{k}_2^{\xi'}, \boldsymbol{p}_{\chi}\rangle$, where a phonon with momentum $\boldsymbol{p}$ and polarization χ is emitted from the first electron, while the other state is $|\Psi_{2,\chi}\rangle = |\boldsymbol{k}_1^{\xi}, \boldsymbol{k}_4^{\xi'}, -\boldsymbol{p}_{\chi}\rangle$, where a phonon with momentum $-\boldsymbol{p}$ and polarization χ is emitted from the second electron. The conservation laws require $\boldsymbol{p} = \boldsymbol{k}_1 - \boldsymbol{k}_3 = \boldsymbol{k}_4 - \boldsymbol{k}_2$ and $\varepsilon_{\boldsymbol{k}_1} + \varepsilon_{\boldsymbol{k}_2} = \varepsilon_{\boldsymbol{k}_3} + \varepsilon_{\boldsymbol{k}_4}$, where $\varepsilon_{\boldsymbol{k}}$ and $|\boldsymbol{k}^{\xi}\rangle$ are the eigenenergy and eigenfunction of H^{ξ}, respectively.

According to the second-order perturbation theory, we calculate the interaction between the two electrons given as

$$\frac{V_{\boldsymbol{k}_1\boldsymbol{k}_2, \boldsymbol{k}_3\boldsymbol{k}_4}^{\xi\xi'}}{N_s \Omega_s} = \sum_{\chi = L, T} \left(\frac{\langle \Psi_f | H_{ep}^{\xi'} | \Psi_{1,\chi}\rangle \langle \Psi_{1,\chi} | H_{ep}^{\xi} | \Psi_i\rangle}{\varepsilon_{\boldsymbol{k}_3} - \varepsilon_{\boldsymbol{k}_1} - \hbar \omega_{\boldsymbol{p}, \chi}} + \frac{\langle \Psi_f | H_{ep}^{\xi} | \Psi_{2,\chi}\rangle \langle \Psi_{2,\chi} | H_{ep}^{\xi'} | \Psi_i\rangle}{\varepsilon_{\boldsymbol{k}_4} - \varepsilon_{\boldsymbol{k}_2} - \hbar \omega_{-\boldsymbol{p}, \chi}} \right). \tag{A2}$$

Previous research [36] shows that the intervalley interaction at low electron density takes the attractive form which is preferable for BCS superconductivity. Hence we focus on the Cooper channel of the interaction where the two electrons have opposite momenta and valley indices, i.e., $\boldsymbol{k}_1 = -\boldsymbol{k}_2 = \boldsymbol{k}$, $\boldsymbol{k}_3 = -\boldsymbol{k}_4 = \boldsymbol{k}'$, and $\xi' = -\xi = \bar{\xi}$. The Cooper channel electron-electron interaction is then

$$\frac{V_{\boldsymbol{k}, \boldsymbol{k}'}}{N_s \Omega_s} = \sum_{\chi = L, T} \frac{\langle \boldsymbol{k}'^{\xi}, -\boldsymbol{k}'^{\bar{\xi}} | H_{ep}^{\bar{\xi}}(\boldsymbol{p}) | \boldsymbol{k}'^{\xi}, -\boldsymbol{k}^{\bar{\xi}}, \boldsymbol{p}_{\chi}\rangle \langle \boldsymbol{k}'^{\xi}, -\boldsymbol{k}^{\bar{\xi}}, \boldsymbol{p}_{\chi} | H_{ep}^{\xi}(\boldsymbol{p}) | \boldsymbol{k}^{\xi}, -\boldsymbol{k}^{\bar{\xi}}\rangle}{\hbar \omega - \hbar \omega_p}$$

$$+ \frac{\langle \boldsymbol{k}'^{\xi}, -\boldsymbol{k}'^{\bar{\xi}} | H_{ep}^{\xi}(\boldsymbol{p}) | \boldsymbol{k}^{\xi}, -\boldsymbol{k}'^{\bar{\xi}}, -\boldsymbol{p}_{\chi}\rangle \langle \boldsymbol{k}^{\xi}, -\boldsymbol{k}'^{\bar{\xi}}, -\boldsymbol{p}_{\chi} | H_{ep}^{\bar{\xi}}(\boldsymbol{p}) | \boldsymbol{k}^{\xi}, -\boldsymbol{k}^{\bar{\xi}}\rangle}{-\hbar \omega - \hbar \omega_p}, \tag{A3}$$

where $\hbar \omega = \varepsilon_{\boldsymbol{k}'} - \varepsilon_{\boldsymbol{k}}$, $\boldsymbol{p} = \boldsymbol{k} - \boldsymbol{k}'$, and we assume $\omega_{\boldsymbol{p}, \chi} = \omega_{-\boldsymbol{p}, \chi} = \omega_p$.

We notice that the matrix elements satisfy

$$\langle \boldsymbol{k}'^{\xi}, -\boldsymbol{k}^{\bar{\xi}}, \boldsymbol{p}_{\chi} | H_{ep}^{\xi}(\boldsymbol{p}) | \boldsymbol{k}^{\xi}, -\boldsymbol{k}^{\bar{\xi}}\rangle = \langle \boldsymbol{k}'^{\xi}, -\boldsymbol{k}'^{\bar{\xi}} | H_{ep}^{\xi}(\boldsymbol{p}) | \boldsymbol{k}^{\xi}, -\boldsymbol{k}'^{\bar{\xi}}, -\boldsymbol{p}_{\chi}\rangle \tag{A4}$$

and

$$\langle \boldsymbol{k}'^{\xi}, -\boldsymbol{k}'^{\bar{\xi}} | H_{ep}^{\bar{\xi}}(\boldsymbol{p}) | \boldsymbol{k}'^{\xi}, -\boldsymbol{k}^{\bar{\xi}}, \boldsymbol{p}_{\chi}\rangle = \langle \boldsymbol{k}^{\xi}, -\boldsymbol{k}'^{\bar{\xi}}, -\boldsymbol{p}_{\chi} | H_{ep}^{\bar{\xi}}(\boldsymbol{p}) | \boldsymbol{k}^{\xi}, -\boldsymbol{k}^{\bar{\xi}}\rangle. \tag{A5}$$

Based on the above expression, we can obtain Eq. (12) in the text.

[1] Y. Cao, V. Fatemi, S. Fang, K. Watanabe, T. Taniguchi, E. Kaxiras, and P. Jarillo-Herrero, Nature (London) **556**, 43 (2018).

[2] Y. Cao, V. Fatemi, A. Demir, S. Fang, S. L. Tomarken, J. Y. Luo, J. D. Sanchez-Yamagishi, K. Watanabe, T. Taniguchi, E. Kaxiras, R. C. Ashoori, and P. Jarillo-Herrero, Nature (London) **556**, 80 (2018).

[3] M. Yankowitz, S. Chen, H. Polshyn, Y. Zhang, K. Watanabe, T. Taniguchi, D. Graf, A. F. Young, and C. R. Dean, Science **363**, 1059 (2019).

[4] X. Lu, P. Stepanov, W. Yang, M. Xie, M. A. Aamir, I. Das, C. Urgell, K. Watanabe, T. Taniguchi, G. Zhang, A. Bachtold, A. H. MacDonald, and D. K. Efetov, Nature (London) **574**, 653 (2019).

[5] J. M. B. Lopes dos Santos, N. M. R. Peres, and A. H. Castro Neto, Phys. Rev. Lett. **99**, 256802 (2007).

[6] G. Li, A. Luican, J. M. B. Lopes dos Santos, A. H. Castro Neto, A. Reina, J. Kong, and E. Y. Andrei, Nat. Phys. **6,** 109 (2010).

[7] D. L. Miller, K. D. Kubista, G. M. Rutter, M. Ruan, W. A. de Heer, P. N. First, and J. A. Stroscio, Phys. Rev. B **81**, 125427 (2010).

[8] A. Luican, G. Li, A. Reina, J. Kong, R. R. Nair, K. S. Novoselov, A. K. Geim, and E. Y. Andrei, Phys. Rev. Lett. **106**, 126802 (2011).

[9] R. Bistritzer and A. H. MacDonald, Proc. Natl. Acad. Sci. USA **108**, 12233 (2011).

[10] J. M. B. Lopes dos Santos, N. M. R. Peres, and A. H. Castro Neto, Phys. Rev. B **86**, 155449 (2012).

[11] P. Moon and M. Koshino, Phys. Rev. B **85**, 195458 (2012).

[12] G. Trambly de Laissardière, D. Mayou, and L. Magaud, Phys. Rev. B **86**, 125413 (2012).

[13] P. Moon and M. Koshino, Phys. Rev. B **87**, 205404 (2013).

[14] M. Koshino and P. Moon, J. Phys. Soc. Jpn. **84**, 121001 (2015).

[15] Y. Xu and G. Jin, Europhys. Lett. **111**, 67006 (2015).

[16] C. Xu and L. Balents, Phys. Rev. Lett. **121**, 087001 (2018).

[17] L. Rademaker and P. Mellado, Phys. Rev. B **98**, 235158 (2018).

[18] J. F. Dodaro, S. A. Kivelson, Y. Schattner, X. Q. Sun, and C. Wang, Phys. Rev. B **98**, 075154 (2018).

[19] F. Wu, T. Lovorn, E. Tutuc, and A. H. MacDonald, Phys. Rev. Lett. **121**, 026402 (2018).

[20] H. C. Po, L. Zou, A. Vishwanath, and T. Senthil, Phys. Rev. X **8**, 031089 (2018).

[21] Y.-Z. You and A. Vishwanath, npj Quantum Mater. **4**, 16 (2019).

[22] H. Isobe, N. F. Q. Yuan, and L. Fu, Phys. Rev. X **8**, 041041 (2018).

[23] C.-C. Liu, L.-D. Zhang, W.-Q. Chen, and F. Yang, Phys. Rev. Lett. **121**, 217001 (2018).

[24] D. M. Kennes, J. Lischner, and C. Karrasch, Phys. Rev. B **98**, 241407(R) (2018).

[25] H. Guo, X. Zhu, S. Feng, and R. T. Scalettar, Phys. Rev. B **97**, 235453 (2018).

[26] K. Seo, V. N. Kotov, and B. Uchoa, Phys. Rev. Lett. **122**, 246402 (2019).

[27] J. M. Park, Y. Cao, K. Watanabe, T. Taniguchi, and P. Jarillo-Herrero, Nature (London) **590**, 249 (2021).

[28] Z. Hao, A. M. Zimmerman, P. Ledwith, E. Khalaf, D. H. Najafabadi, K. Watanabe, T. Taniguchi, A. Vishwanath, and P. Kim, Science **371**, 1133 (2021).

[29] Y. Cao, J. M. Park, K. Watanabe, T. Taniguchi, and P. Jarillo-Herrero, Nature (London) **595**, 526 (2021).

[30] P. Stepanov, I. Das, X. Lu, A. Fahimniya, K. Watanabe, T. Taniguchi, F. H. L. Koppens, J. Lischner, L. Levitov, and D. K. Efetov, Nature (London) **583**, 375 (2020).

[31] Y. Saito, J. Ge, K. Watanabe, T. Taniguchi, and A. F. Young, Nat. Phys. **16**, 926 (2020).

[32] H. S. Arora, R. Polski, Y. Zhang, A. Thomson, Y. Choi, H. Kim, Z. Lin, I. Z. Wilson, X. Xu, J. H. Chu, K. Watanabe, T. Taniguchi, J. Alicea, and S. Nadj-Perge, Nature (London) **583**, 379 (2020).

[33] X. Liu, Z. Wang, K. Watanabe, T. Taniguchi, O. Vafek, and J. I. A. Li, Science **371**, 1261 (2021).

[34] F. Wu, A. H. MacDonald, and I. Martin, Phys. Rev. Lett. **121**, 257001 (2018).

[35] F. Wu, E. Hwang, and S. Das Sarma, Phys. Rev. B **99**, 165112 (2019).

[36] B. Lian, Z. Wang, and B. A. Bernevig, Phys. Rev. Lett. **122**, 257002 (2019).

[37] Y. W. Choi and H. J. Choi, Phys. Rev. Lett. **127**, 167001 (2021).

[38] Y.-Z. Chou, F. Wu, J. D. Sau, and S. Das Sarma, Phys. Rev. Lett. **127**, 187001 (2021).

[39] V. T. Phong, P. A. Pantaleón, T. Cea, and F. Guinea, Phys. Rev. B **104**, L121116 (2021).

[40] Y.-Z. Chou, F. Wu, J. D. Sau, and S. Das Sarma, Phys. Rev. Lett. **127**, 217001 (2021).

[41] J. Cao, F. Qi, H. Yang, and G. Jin, Phys. Rev. B **101**, 155419 (2020).

[42] Y. Zhang, Y. Gao, and D. Xiao, Phys. Rev. B **101**, 041410(R) (2020).

[43] M. Fujimoto, H. Koschke, and M. Koshino, Phys. Rev. B **101**, 041112(R) (2020).

[44] Y. Su and S.-Z. Lin, Phys. Rev. B **101**, 041113(R) (2020).

[45] A. I. Cocemasov, D. L. Nika, and A. A. Balandin, Phys. Rev. B **88**, 035428 (2013).

[46] M. Koshino and Y.-W. Son, Phys. Rev. B **100**, 075416 (2019).

[47] F. Wu and S. Das Sarma, Phys. Rev. B **101**, 155149 (2020).

[48] J. A. Sauls, Adv. Phys. **43**, 113 (1994).

[49] G. Yang and K. Maki, Europhys. Lett. **48**, 208 (1999).

[50] H. Goudarzi, M. Khezerlou, H. Sedghi, and A. Ghorbai, Superlattices Microstruct. **104**, 1 (2017).

[51] L. Mao, J. Shi, Q. Niu, and C. Zhang, Phys. Rev. Lett. **106**, 157003 (2011).

[52] S. Hesselmann, D. D. Scherer, M. M. Scherer, and S. Wessel, Phys. Rev. B **98**, 045142 (2018).

[53] T. Cea, N. R. Walet, and F. Guinea, Phys. Rev. B **100**, 205113 (2019).